Kinetic turbulence in fast three-dimensional collisionless guide-field magnetic reconnection

P. A. Muñoz[*,†] and J. Büchner[†]
Max-Planck-Institut für Sonnensystemforschung, D-37077 Göttingen, Germany

(Received 27 January 2017; revised manuscript received 9 August 2018; published 23 October 2018)

Although turbulence has been conjectured to be important for magnetic reconnection, still very little is known about its role in collisionless plasmas. Previous attempts to quantify the effect of turbulence on reconnection usually prescribed Alfvénic or other low-frequency fluctuations or investigated collisionless kinetic effects in just two-dimensional configurations and antiparallel magnetic fields. In view of this, we analyzed the kinetic turbulence self-generated by three-dimensional guide-field reconnection through force-free current sheets in frequency and wave-number spaces, utilizing 3D particle-in cell code numerical simulations. Our investigations reveal reconnection rates and kinetic turbulence with features similar to those obtained by current *in situ* spacecraft observations of MMS as well as in the laboratory reconnection experiments MRX, VTF, and VINETA-II. In particular, we found that the kinetic turbulence developing in the course of 3D guide-field reconnection exhibits a broadband power-law spectrum extending beyond the lower-hybrid frequency and up to the electron frequencies. In the frequency space the spectral index of the turbulence appeared to be close to -2.8 at the reconnection X line. In the wave-number space it also becomes -2.8 as soon as the normalized reconnection rate reaches 0.1. The broadband kinetic turbulence is mainly due to current-streaming and electron-flow-shear instabilities excited in the sufficiently thin current sheets of kinetic reconnection. The growth of the kinetic turbulence corresponds to high reconnection rates which exceed those of fast laminar, nonturbulent reconnection.

DOI: 10.1103/PhysRevE.98.043205

I. INTRODUCTION

Magnetic reconnection is a fundamental process that converts magnetic energy into kinetic energy and heat in laboratory, space, and astrophysical plasmas [1,2]. Though ubiquitous in the collisionless plasmas of the Universe, it is not clear, yet, whether and which turbulence can enhance the energy conversion by reconnection. In the past it has been conjectured that macroscopic (fluid) turbulence can enhance the reconnection rate [3,4]. But the role of kinetic turbulence in collisionless magnetic reconnection is much less explored. Indeed, as is well known, current sheets (CSs), through which magnetic reconnection takes place, contain a sufficient amount of free energy which in collisionless plasmas is released by instabilities at the smallest, kinetic scales. In contrast to fluid [magnetohydrodynamics (MHD)] turbulence, the universality and properties of collisionless turbulence self-generated by magnetic reconnection, such as their scaling, power-law spectral index, and spectral breaks, are not yet well understood.

Recent *in situ* measurements often detected thin current sheets formed in the turbulent space plasmas of the solar wind or Earth's magnetosheath, leading to magnetic reconnection events generating heating and dissipation [5–14]. The small-scale turbulence in the vicinity of those CSs can usually be associated to spectral breaks in the magnetic fluctuation spectra near the ion cyclotron frequency Ω_{ci}. At larger scales (low frequencies), there is the characteristic inertial range of the turbulent cascade, while above ion scales the turbulent spectra shows a clear power law with spectral indices close to -2.7 [15,16]. However, the power laws and spectral breaks near CSs are very similar to those measured in homogeneous turbulent solar wind plasmas [15,17,18], and that is why it is not well known how much reconnection contributes to the measured spectra. In addition, the spectral breaks might not be universal and depend on several parameters [19–23]. Note that similar spectra, but with different spectral indices, were also obtained for other quantities such as the electric field [24–27], density [28–30], and higher-order momenta of the distribution functions such as bulk flow velocity and temperature [31–33]. On the other hand, laboratory experiments of magnetic reconnection (MRX, VTF, VINETA-II) obtained turbulent cascades as well but with different spectral indices and spectral breaks near the lower-hybrid frequency $\Omega_{\rm LH} = \omega_{pi}/\sqrt{1+\omega_{pe}^2/\Omega_{ce}^2}$ (where ω_{pe} (ω_{pi}) is the electron (ion) plasma frequency and Ω_{ce} is the electron cyclotron frequency) [34–36]. These different spectral breaks indicate a change in the physical nature of turbulence, depending only on the ions (in space plasmas) or with an influence of the electrons (in laboratory plasmas). In space, the first spectral break observed in steady and homogeneous solar wind turbulence is usually explained by a turbulent cascade of kinetic Alfvén waves (KAW) [37,38], whistler waves [39], Landau damping [37,40,41], ion cyclotron damping [42], or combinations of these mechanisms depending on parameters such as the plasma β [22]. There is even some evidence from measurements of homogeneous turbulence in the solar

[*]munozp@mps.mpg.de
[†]Also at Max-Planck/Princeton Center for Plasma Physics, Princeton University, Princeton, NJ 08543, USA; Now at EW 215, Center for Astronomy and Astrophysics, Technical University Berlin, Hardenbergstrasse 36, 10623 Berlin, Germany.

wind of a second spectral break near electron scales and a steeper power-law spectral index beyond it [43–45]. However, measurements at those high electron frequencies are more difficult to obtain due to the instrumental limitations, and other interpretations such as an exponential cutoff beyond electron scales have also been proposed [17].

It is important to mention, however, that all those spectra measurements in space plasmas are performed in the spacecraft frame of reference, which gives a Doppler-shifted frequency $\omega_{sc} = \omega + \vec{k}\cdot\vec{v}_{sw}$, where $\vec{v}_{sw}$ is the plasma flow (solar wind) speed. In order to compare with theoretical predictions in the plasma frame of reference, a transformation has to be carried out to the wave-number domain $\vec{k}$ by assuming the validity of Taylor's hypothesis [46] $\omega \ll \vec{k}\cdot\vec{v}_{sw}$. This implies a linear relationship between the spacecraft frequency space and the wave-number domain in the plasma frame $k = \omega_{sc}/(|v_{sw}|\cos\theta)$, while the frequency spectrum in the plasma frame ω remains unknown. In the last expression, θ is the angle between the wave number $\vec{k}$ and solar wind velocity $\vec{v}_{sw}$, i.e., $\vec{k}\cdot\vec{v}_{sw} = k|\vec{v}_{sw}|\cos\theta$. This hypothesis is not valid for slow plasma flows or for high-frequency dispersive waves with a nonlinear relation with the wave number [47,48].

Another important point related to terminology is that electron scales in spacecraft measurements have a slightly different meaning than in a pure frequency analysis in the plasma frame. This is because it refers to the wave number kd_e (electron skin depth) mapped to the frequency space by using the previously discussed Taylor's hypothesis, resulting in $\omega_{de} = v_{sw}/d_e$. This frequency is closer to the corresponding ion scales $\omega_{di} = v_{sw}/d_i$ (mapping of the wave number related to the ion skin depth kd_i) by a factor of the square root of the mass ratio $\sqrt{m_i/m_e}$ (also valid for the electron (ion) gyroradius $k\rho_e$ ($k\rho_i$) compared to a direct frequency spectra, where the ion and electron frequencies Ω_{ci} and Ω_{ce} are separated by m_i/m_e.

The properties of stationary and homogeneous kinetic turbulence leading to localized magnetic reconnection were numerically investigated using hybrid-PIC (particle-in-cell), gyrokinetic, or Vlasov codes simulations [49–58]. These investigations showed that ion-scale CSs, where magnetic reconnection can take place, can form from decaying or driven turbulence, leading to heating, temperature anisotropies, and dissipation. Fully-kinetic PIC-code simulations of shear-driven or decaying turbulence demonstrated that CSs also form at electron scales and contribute to the turbulent spectra [59–64]. A recent comparison of shear-driven turbulence with different physical and numerical models also showed the formation of current sheets and hinted towards the importance of reconnection in turbulence at different scales [65]. The idea that magnetic reconnection can have an important contribution to turbulence has also been suggested by a number of recent theoretical works in both collisional and collisionless regimes [66–71] (see also the review [72]). In spite of all those works assessing the role of multiple magnetic reconnection events in turbulence, the opposite problem of the turbulence generated by magnetic reconnection in a single isolated current sheet has been rarely characterized. Although there has been some work analyzing the turbulence generated by plasmoid magnetic reconnection within the MHD framework [73], the self-generated turbulence due to kinetic instabilities in collisionless magnetic reconnection is much less known. For example, [74] is one of the few studies analyzing this problem using 3D fully-kinetic PIC-code simulations of reconnection, revealing the presence of non-Gaussian statistics and multifractal structures associated with intermittency and dissipation. Note that all these simulations usually revealed the spatial turbulence spectra, while the also relevant frequency spectrum have remained mostly unknown, which is one of the purposes of this study.

On the other hand, the properties of instabilities in CSs and their consequences for the kinetic turbulence generated during magnetic reconnection were also investigated by using 3D PIC-code [75] or fully-kinetic 3D Vlasov-code simulations [76,77]. In particular, the role of Buneman instability was studied with Vlasov codes [78,79]. This instability is relevant to understand the consequences of the self-generated turbulence in reconnection, because it can produce anomalous resistivity and thus balance the reconnection electric field associated to magnetic reconnection [80,81]. Even though in 2.5D fully-kinetic reconnection simulations this anomalous resistivity could not be found [82], other 3D fully-kinetic reconnection simulations provided some positive evidence [80,83–86].

Although we do not attempt to make a direct comparison with spacecraft measurements or check the validity of Taylor's hypothesis under realistic conditions, the need to study the properties of both the frequency and wave-number spectra at kinetic and dispersive scales generated by magnetic reconnection is clear. In collisionless plasmas, the high-frequency kinetic turbulence is essential for the balance of electric fields, and therefore for the rate of magnetic reconnection, for energy dissipation and heating [87].

II. SIMULATIONS

We investigated the kinetic turbulence, self-generated in 3D collisionless reconnection, and its consequences for the reconnection rate, considering force-free equilibrium current sheets. Those are closer to real and astrophysical CSs rather than Harris-type CSs, which require strong pressure gradients. In force-free CSs with a guide field in the current (our z) direction, the magnetic pressure is balanced by an electron shear flow in the x direction, while the thermal pressure is constant (see specific setup in [88]). We used the 3D fully-kinetic PIC-code ACRONYM [89]. We illustrate our findings by presenting the results of a simulation run with an ion to electron mass ratio $m_i/m_e = 100$, initially equal electron and ion temperatures ($T_i/T_e = 1.0$), a plasma beta $\beta_e = \beta_i = 2\mu_0 n_0 k_B T_i/B_T^2 = 0.016$, a ratio of the electron thermal speed to the speed of light of $v_{\mathrm{th},e}/c = 0.1$ and a relative guide-field strength $b_g = B_g/B_{\infty y} = 2$, where $B_{\infty y}$ is the asymptotic magnetic field (often abbreviated here as B_0). The initial total magnetic field $B_T = B_{\infty y}\sqrt{1+b_g^2}$ is constant, as well as the ion and electron number densities $n_0 = n_i = n_e$. Note that the plasma beta on the asymptotic magnetic field and guide fields are, respectively, $\beta_{e,B\infty y} = \beta_{i,B\infty y} = 0.08$ and $\beta_{e,Bg} = \beta_{i,Bg} = 0.02$. Here, $v_{\mathrm{th},e} = \sqrt{k_B T_e/m_e}$ ($v_{\mathrm{th},i} = \sqrt{k_B T_i/m_i}$), and therefore the electron (ion) Larmor radius on the total magnetic field is $\rho_e = v_{\mathrm{th},e}/\Omega_{ce,BT} = (\sqrt{k_B T_e/m_e})/(eB_T/m_e)$ ($\rho_i =$

$v_{\mathrm{th},i}/\Omega_{ci,BT} = (\sqrt{k_B T_i}/m_i)/(eB_T/m_i))$. This definition leads to a ratio of characteristic length scales $\rho_i/d_e = 0.89$. The current sheet halfwidth is $L = 0.25d_i$.

In the case further discussed here the number of particles per cell (ppc) was 200 (100 per specie), with a total of 2.7×10^{10} particles in the simulation box. The simulation box covers a domain $L_x\times L_y\times L_z = 4d_i\times8d_i\times16d_i$, where $d_i = c/\omega_{\mathrm{pi}}$ is the ion inertial length (ω_{pi} is the ion plasma frequency). The calculations were carried out on a mesh containing $256\times512\times1024$ grid points. Periodic boundary conditions were chosen since we simulated two equivalent but oppositely directed current sheet flows. For comparison with other studies of turbulence in the wave-number domain, our system allows the following minimum and maximum value of wave numbers: $k_\parallel d_i = [0.392 - 201]$ (or $k_\parallel\rho_i = [0.035 - 17.98]$) and $k_\perp d_i = [0.785 - 201]$ (or $k_\perp\rho_i = [0.07 - 17.98]$). Here $k_\parallel = k_z$ (out-of-reconnection-plane direction, because of the dominant guide field) and $k_\perp = k_y$ (along the reconnected component of the magnetic field).

Reconnection is triggered by an initial magnetic field perturbation with amplitude $0.07B_{\infty y}$ for the corresponding magnetic field components (B_x and B_y). This perturbation is narrowly localized in the current direction around $z = L_z/2$ and with a long wavelength tearing mode in the y direction, generating a three-dimensional X point.

III. EVOLUTION OF TURBULENCE IN RECONNECTION

Figure 1 depicts the spatial distribution of the current density distribution j_z in the plane $z = L_z/2$ at $t = 13.5\Omega_{ci}^{-1}$, after reconnection has fully developed. The figure illustrates the well-known asymmetric structure of finite guide-field reconnection and the spatial structure of turbulence. Figure 2 shows the reconnection rate numerically calculated in two different ways, which, by definition, should be identical, both characterizing the efficiency of reconnection. $d\psi/dt$ (red solid line) is the rate of change of the total magnetic flux calculated across a rectangle formed by the X and O lines of reconnection and the lines connecting $y = L_y/2$ and $y = 0$.

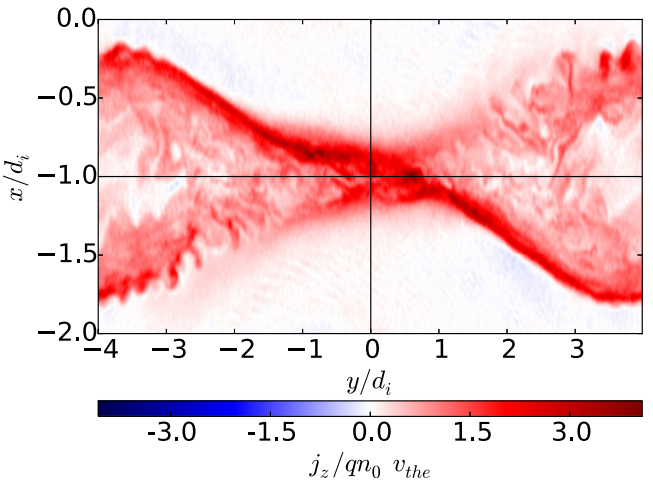

FIG. 1. Spatial distribution of the current density j_z at $t = 13.5\Omega_{ci}^{-1}$ in the x-y plane through $z = L_z/2$.

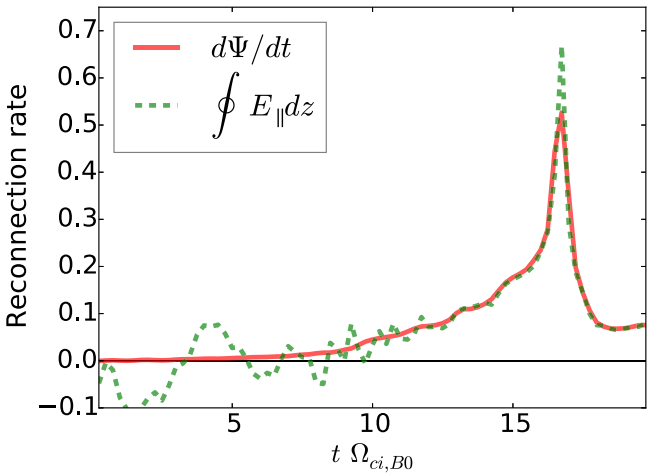

FIG. 2. Reconnection rate (normalized to $B_{\infty y}V_A/c$, with V_A is the Alfvén speed on $B_{\infty y}$) calculated as the derivative of the reconnected flux between the X and O point of reconnection $d\psi/dt$ (red solid line), and as the parallel electric field integrated along the perimeter of the same region $\oint E_\parallel dz$ (green dashed line).

This quantity should be equal to $\oint E_\parallel dz$ (with $E_\parallel = \vec{E}\cdot\vec{B}/B$) represented with a green dashed line, the parallel electric field integrated along the perimeter of the same rectangle. The deviation between the two quantities is due to numerical errors caused by the PIC-code shot noise, which affects more the determination of the electric field rather than other quantities. As Fig. 2 illustrates, reconnection starts to grow significantly only after $t \sim 10\Omega_{ci}^{-1}$ reaches the limit of fast Petschek reconnection (0.1 in normalized units) at $t \sim 13\Omega_{ci}^{-1}$, and further grows doubling that rate by $t = 15\Omega_{ci}^{-1}$. But the peak at $t = 16.5\Omega_{ci}^{-1}$, with values of the reconnection rates as high as $0.5V_AB_{\infty y}$, is not due to only reconnection at the X line, but also due to the effects of the periodic boundary conditions: the second current sheet starts to interact with the first current sheet (the one studied here). One effect of this is that the boundary of the magnetic island of the second current sheet is next to the X line of the first one, limiting their growth and causing strong instabilities at the contact points due to the counterstreaming flows and possibly secondary reconnection sites. A second effect is that the available magnetic flux incoming to each current sheet is drastically reduced, throttling the reconnection rates by a large amount. In particular, the latter effect can be seen after $t \approx 16.5\Omega_{ci}^{-1}$ in Fig. 2, displaying a sharp decrease in the reconnection rates to values below $0.1V_AB_{\infty y}$. By $t \approx 18\Omega_{ci}^{-1}$ all the available magnetic flux is already exhausted and after $t \approx (20\text{–}21)\Omega_{ci}^{-1}$ reconnection stops. Because of this, all the processes after $t \approx 15\Omega_{ci}^{-1}$ should already be affected by the direct interaction between the two current sheets and are not representative of single X-line reconnection. Note that the described evolution of reconnection in this system is dependent on the simulation box size, especially along the current direction (z). The reconnection onset and peak values of the reconnection rate are reached later for longer boxes and the whole reconnection process is longer if the system is long enough along the current direction.

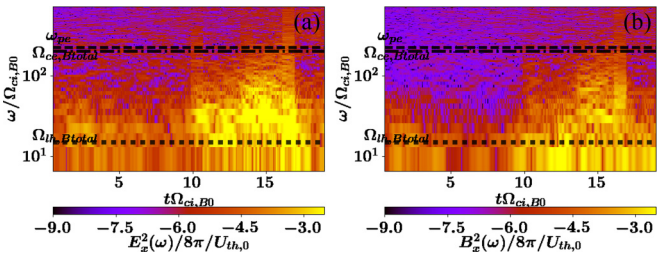

FIG. 3. Temporal evolution of the spectra as a time-frequency representation (spectrogram) of the perpendicular electric E_x^2 (b) and magnetic B_x^2 (b) fluctuations at the X point of reconnection. Quantities are normalized to $U_{\mathrm{th},0} = (3/2)n_0 k_B T_{e,0}$. The characteristic plasma frequencies are indicated by black horizontal dotted (Ω_{LH}), dashed-dotted (Ω_{ce}), and dashed (ω_{pe}) lines.

The dynamic spectrum of the turbulence is depicted by Fig. 3, which shows the temporal evolution of the frequency spectrum of electric and magnetic fields in the direction perpendicular to the current flow direction at the X point of reconnection. We obtained them by a short-time Fourier transform using a sliding Tukey window with an appropriate overlap and plotted as spectrograms. Figure 3 shows that until about $t = 10\Omega_{ci}^{-1}$, significant turbulence is developed only below the lower-hybrid frequency Ω_{LH}. After that time both electric and magnetic turbulence strongly increase at kinetic scales up to the electron frequencies. The turbulence broadening correlates well with the enhanced reconnection rates (cf. Fig. 2).

IV. FREQUENCY SPECTRA

In Fig. 4, we show the resulting frequency spectra of the perpendicular magnetic field fluctuations B_x at the X line during two different characteristic time intervals: $t\Omega_{ci} = 1$–5 and $t\Omega_{ci} = 11$–15. In order to diminish the noise level, we bin

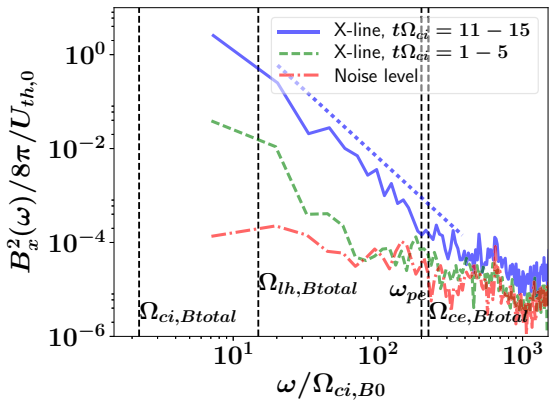

FIG. 4. Spectrum of perpendicular magnetic field fluctuations B_x^2 at the reconnection X point, for two time intervals. The raw simulation data is binned (see main text for details). The power spectra are normalized to $U_{\mathrm{th},0} = (3/2)n_0 k_B T_{e,0}$. The numerical noise level is shown for comparison. The black dashed vertical lines indicate characteristic plasma frequencies. The diagonal dashed blue line represents the linear fit with spectral slope −2.8 of the continuous blue curve, within the indicated frequency range.

the raw simulation data and averaging every eight data points (for both frequency and spectral power). This is equivalent to an average over an interval of $14\Omega_{ci,B0}$. Note that by binning the simulation data, the minimum resolved frequency becomes larger, and closer to the lower-hybrid frequency Ω_{LH}. But it does not modify the spectral slope above Ω_{LH}, which is our main interest here.

The comparison of these two spectra at the intervals $t\Omega_{ci} = 1$–5 and $t\Omega_{ci} = 11$–15 clearly demonstrates the development of the high-frequency kinetic scale turbulence above the lower-hybrid frequency but also an enhanced spectral power close to Ω_{LH}. Note that Fig. 4 also shows the spectrum of the (numerical) shot noise of the magnetic fluctuations (red line) due to the finite number of particles used in the PIC-code simulations. This noise spectrum was obtained at a location away from the CSs. The plot indicates that fluctuations at frequencies above ω_{pe} and Ω_{ce} (more specifically, above $\omega \gtrsim 400\Omega_{ci,B0}$), shown as dashed vertical lines, are due to numerical effects, while the turbulence below these electron frequencies significantly exceeds the numerical noise level. Above Ω_{LH}, however, a clear steep power-law spectrum $P = \omega^{\alpha}$ develops, with a spectral index $\alpha \approx -2.83$ which extends up to the electron frequencies ω_{pe} and Ω_{ce}. More precisely, we calculated the spectral index by means of a least squares linear fit in the frequency range $\omega/\Omega_{ci,B0} = 17$–$400$ (for the interval $t\Omega_{ci} = 11$–15), in order to consider all the frequency range above Ω_{LH} until the numerical noise level. This reference spectral slope and its associated range is indicated as a dashed blue line in Fig. 4. See Appendix for a discussion about the effects of the particle number and the choice of frequency range for the fitting on those results.

Note that in contrast to the usually used simpler spatial structure analysis of the turbulence, we used a direct time-frequency-domain diagnostic of high cadence simulation data by a stationary virtual probe located at the X point of reconnection, which provides the simplest and most general way of analyzing the frequency turbulent spectra in this system. This approach provides different insights in those kind of simulations, while related work by [90,91] analyzed the frequency spectra in homogeneous turbulence simulations. Although this spectral index −2.8 is often measured by spacecrafts in turbulent space plasmas undergoing reconnection between ion and electron scales (roughly the frequency-mapped kd_i to kd_e by assuming Taylor's hypothesis) [10,15], a direct comparison is not appropriate, because the spacecrafts are always in relative motion with respect to the plasma frame. Instead, our method to obtain frequency spectra actually compares better with laboratory experiments, where their probes are stationary. Furthermore, the compared range is not the same between simulations and space observations: the lower-hybrid frequency is usually above the typical frequency range accessible by space instruments, since it approximately coincides with the location of the second spectral break (at the frequency-mapped kd_e) if the frequency mapped kd_i is close to Ω_{ci} [43–45]. Nevertheless, this range of frequencies is more easily accessible in laboratory experiments, which reveal a spectral break and a steep power law above Ω_{LH} [34–36].

Note that it is important to obtain independently both frequency and wave-number spectra of fluctuations in order to get the plasmas dispersive properties without any preliminary

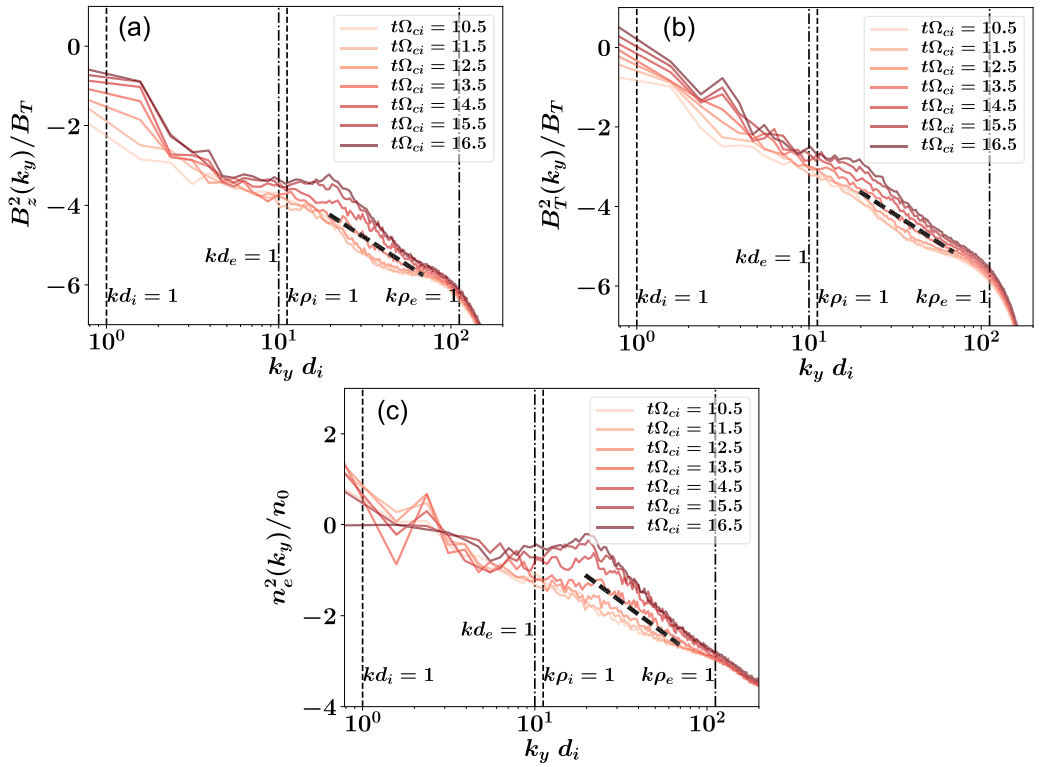

FIG. 5. Spectral slopes of the k_y power spectra for different times (in the range $t\Omega_{ci} = 10.5$–16.5) and different physical quantities. (a) B_z^2 magnetic field. (b) Total magnetic field B_T^2. (c) n_e^2 electron density. The dashed oblique straight line indicates the reference slope $\alpha = -2.8$.

assumption such as Taylor's hypothesis, which might not apply for high-frequency dispersive waves, as in our simulations. In view of this, we also calculated the spatial spectra in our simulations. Thus, we can make a proper comparison with our resulting frequency spectra, as well as to previous studies and observations or measurements.

V. WAVE-NUMBER SPECTRA

The results for the calculation of the wave-number spectra at the center of the left CS $x = -1.0d_i$ and along the y direction are shown in Fig. 5. These figures show the power spectral density (PSD) of the fluctuations in the parallel magnetic field $B_z^2(k_y)$ (a), total magnetic field $B_T^2(k_y) = B_x^2(k_y) + B_y^2(k_y) + B_z^2(k_y)$ (b), and electron density $n_e^2(k_y)$ (c). Each wave-number spectra is averaged along the out-of-plane direction z. Common features for the magnetic field and density spectra are the monotonously increasing spectral power as the times goes by, a bump beyond $k = \rho_i^{-1}$ (more precisely, at $kd_i \sim 20$), in particular for δn_e and δB_T, and a numerical steepening close to the grid scales for $k\rho_e > 1$.

Between $k\rho_i = 1$ and $k\rho_e = 1$, there are some ranges where a straight line can be fitted. Therefore, we calculate spectral slopes α using a least squares linear fit of $P = k^\alpha$ for all the available wave-number data in a given range. It is clear from Fig. 5 that those k-spectral indices are dynamical quantities depending on time, loosely correlated with the value of the reconnection rate. For reference, we indicate by a black dashed line the reference slope -2.8 close to the spectra obtained at $t\Omega_{ci} = 13.5$. The plots demonstrate a good fit in the wave-number range $kd_i = 20$–80. For earlier times, the range for the linear fitting is moved to smaller wave numbers, $kd_i = 10$–35, because there is a clear flattening of the spectra at about $kd_i \sim 40$, in particular of the B_z component of the magnetic field fluctuations. For late times ($t\Omega_{ci} \gtrsim 13.5$), we use the wave-number range $kd_i = 20$–80 for the linear fitting, since this includes the wave numbers above the bump beyond $k\rho_i \geqslant 1$, where the spectra corresponds to a straight line.

The variation of the spectral indices with time is summarized by Fig. 6. This figure shows that the slope of the electron density fluctuations continuously steepens with time [see also Fig. 5(c)], reaching a maximum of $\alpha \approx -3.7$ at

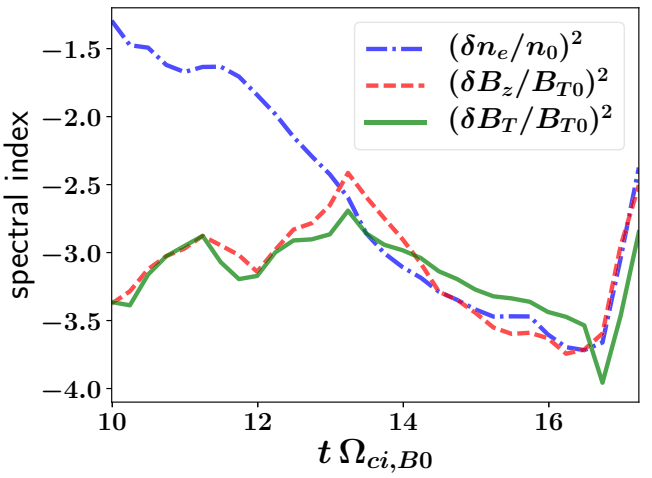

FIG. 6. Spectral slopes of the k_y spectra for different times and different physical quantities.

$t\Omega_{ci} \approx 16.5$. At this time the reconnection rate is maximum until it becomes determined by the interaction of the two current sheets in the simulation domain. Meanwhile, the parallel and total magnetic field fluctuations flatten until $t\Omega_{ci} \approx 13.2$. Later they steepen again, with similar spectral indices, and are also comparable in power to the electron density fluctuations. Close to $t\Omega_{ci} \approx 13.2$, the spectral indices reach the range $\alpha = [-2.8, -2.5]$. At this same time, the normalized reconnection rate becomes 0.1 (cf. Fig. 2). The spectral indices become $\alpha = [-3.5, -3.3]$ at $t\Omega_{ci} \approx 15$, where the energy conversion rate is ~ 0.2 (normalized reconnection rate), before reconnection becomes affected by the second current sheet in the simulation domain at $t\Omega_{ci} \approx 16.5$.

Therefore, the varying value of these spectral index slopes in the wave-number domain probably indicates that the kind of turbulence developed due to nonsteady reconnection, dominated by instabilities, also changes during the course of reconnection.

We also analyzed the wave-number spectra of density and magnetic fluctuations along the out-of-plane direction z (mostly aligned with the dominant guide field) in the region near the X line. A similar analysis also reveals power-law spectra with similar variable spectral indices (and in approximately the same range). Those wave-number spectra, however, do not show a clear spectral break near $k\rho_i = 1$ and they also display a shorter turbulent cascade when no spatial average is used (plots not shown here), since the noise level is higher. Note that if an average of the wave-number spectra in k_z along the current sheet (y direction) would be performed, it would make to distinguish and fit a power law more difficult, since the inhomogeneity and general features of turbulence in the outflow region are very different from those near the X line, averaging out different kinds of processes. In contrast, an average of the power spectral in k_y along z (the one used here) is more consistent because it is similar among different slices.

The spatial spectral indices of the self-generated magnetic turbulence along the CS are similar to those measured in space plasmas close to $\alpha = -2.7$, but only when the (normalized) reconnection rates are close to 0.1. Those spectral indices in the wave-number domain are also within the same range as the frequency spectral slope measured here for a stationary probe at the X point (see Fig. 4). However, this similar slope in ω and k_y does not necessarily indicate the presence of nondispersive waves with a linear dependence between ω and k_y, since we verified that the ω spectrum is different in the outflow regions of reconnection: far from the X line, there is less turbulence and, therefore, the magnetic frequency spectrum does not develop a spectral index as steep as in the X line. Since the k_y spectrum considers equally all these regions with different properties in the ω domain, a dispersion relation ω-k_y cannot be inferred uniquely from a single sampling point in time. Moreover, based on different two-dimensional (2D) simulations for a similar parameter range (with a higher output cadence), dispersion relations ω-k_y hint to the presence of dispersive waves in the whistler branch with a quadratic dependence $\omega \propto k_y^2$. Nevertheless, more work is needed to clarify if the similarity of ω and k_y spectral indices is the result of our parameter range or a more generic characteristic of this kind of turbulent system.

One of the goals of other works analyzing the turbulence at kinetic scales is identifying whether the turbulent fluctuations can be classified as due to KAW or whistler waves [18,41,92]. The identification criteria is based on asymptotic formulas leading to dispersion relations and associated transport ratios related to the compressibility of fluctuations. However, those expressions require $\omega \ll k_\perp v_{\mathrm{th},i}$ for KAW and $k_\perp v_{\mathrm{th},i} \ll \omega \ll k_z v_{\mathrm{th},e}$ for whistler waves (see Fig. 1 of Ref. [41]), which are not well satisfied in our case. One of the most important reasons is that many of those formulas are derived for conditions $\beta \sim 1$, which do not apply well in our simulations with small plasma β, in addition to the use of an artificially small mass ratio and simulation domain sizes.

VI. INSTABILITIES LEADING TO TURBULENCE

The broadband turbulence at the X line self-generated by reconnection, enhancing the spectral power between the lower-hybrid and electron frequencies, is caused mainly by a (streaming) Buneman instability [93]. The source of free energy of this instability is the relative streaming of the current-carrying electrons with respect to the ions. We verified this conjecture by investigating the evolution of the drift speed $V_{\mathrm{rel},z}$ along the X line of reconnection, with $V_{\mathrm{rel},z} = V_{i,z} - V_{e,z}$, where $V_{i,z}$ ($V_{e,z}$) is the ion (electron) drift speeds along z. As one can see in Fig. 7(a), initially, in the thin CS $V_{\mathrm{rel},z}$ already slightly exceeds the initial electron thermal speed $v_{\mathrm{th},e}$. This causes an initial (parallel) plasma heating, i.e., the electron thermal speed $v_{\mathrm{th},e,z}$ increases. The marginal Buneman instability criterion $V_{\mathrm{rel},z} \sim v_{\mathrm{th},e,z}$, however, is not reached again until $t \sim 9\Omega_{ci}^{-1}$. This way $V_{\mathrm{rel},z}/v_{\mathrm{th},e,z}$ can again increase above the threshold of the Buneman instability. Exactly at that time the broadband kinetic turbulence starts to develop. After that the electron heating continues while the electron-ion drift speed now grows even faster than the

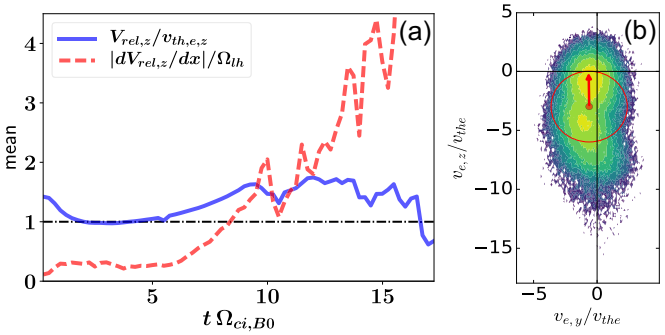

FIG. 7. (a) Time histories of quantities associated to streaming $V_{\mathrm{rel},z}$ (solid line) and shear flow $|dV_{\mathrm{rel},z}/dx|$ (dashed line) instabilities. The diagnostic corresponds to their mean value along the X line of reconnection (average along the z direction). The horizontal dashed line depicts a lower-order estimation of the threshold of the Buneman instability. (b) Electron distribution function in the plane v_y-v_z, taken at the X line and near $L_z/2$, in a cubic region of size $0.1d_i \times 0.3d_i \times 1.0d_i$. The red arrow indicates the direction of the local magnetic field centered at the local bulk drift speed (red point). The red circle has a radius of $3v_{\mathrm{th},e}$, indicating approximately the initial distribution (99.7% of the particles are inside of three standard deviations for a drifting Maxwellian with thermal spread equal to $v_{\mathrm{th},e}$).

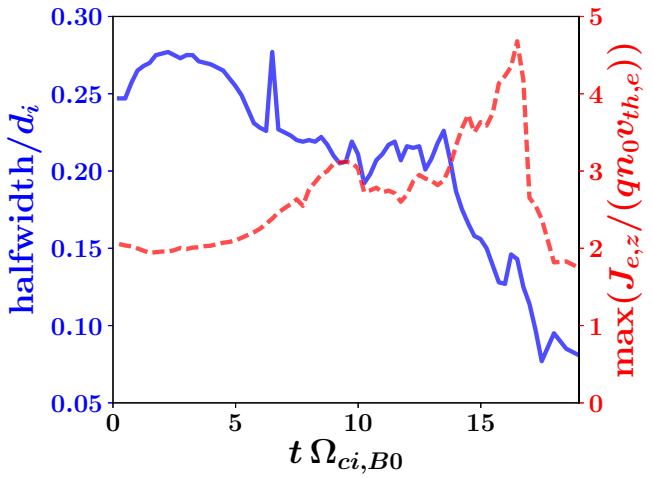

FIG. 8. Time history of two characteristic quantities related to the current sheet evolution, calculated at the center $y = 0, x = -1d_i$. Blue continuous line: current sheet halfwidth (values in the left axis). Red dashed line: maximum of $J_{e,z}$ (values in the right axis). See further details in the text.

electron thermal velocity. This keeps the CS Buneman unstable until boundary effects start to play a significant role close to $t\Omega_{ci} \sim 16.5$. Note that previous 3D magnetic reconnection studies reported similar Buneman-type instabilities and the generation of current filaments in the current density along the z direction [80,83]. The Buneman streaming instability is not effective in 2.5D magnetic reconnection in which, therefore, no high-frequency turbulence near $\Omega_{\rm LH}$ develops [94].

As a second contribution to the broadband kinetic turbulence, which also enhances reconnection, an electron shear flow instability is excited at the reconnection site. Figure 7(a) shows the gradient of the current-aligned electron flow across the CS, $dV_{e,z}/dx$. It strongly grows after $t\Omega_{ci} \gtrsim 13$ when it exceeds the threshold of the electron-ion hybrid (EIH) instability $dV_{e,z}/dx \gg \Omega_{\rm LH}$ [95,96]. The EIH instability is a kinetic branch of the Kelvin-Helmholtz instability which enhances the plasma turbulence near the lower-hybrid frequency. The kinetic shear flow instability criterion is fulfilled, however, only after the Buneman streaming instability has already developed.

The most active period of both instabilities ($t\Omega_{ci} \gtrsim 13.5$), described above, it is also correlated with a fast thinning of the current sheet. Figure 8 shows the evolution of the halfwidth and maximum of the electron current density $J_{e,z}$. We choose to diagnose this quantity and not J_z because most of the current is carried by the electrons, both initially and also later during the course of the CS evolution. An ion current sheet also forms self-consistently, but its contribution to the total current is much smaller and it is also much broader. We calculate the quantities shown in Fig. 8 in the x-y reconnection plane along a cut in the x direction through the center of the first current sheet ($y = 0$). This is approximately the location of the X point. We also average $J_{e,z}(x, y)$ along the out-of-plane direction z. Thus, the maximum value of the average $\bar{J}_{e,z}(x, y)$ is obtained from calculations along this cut as shown in Fig. 8 (the red dashed line). On the other hand, we fit the function $f(x) = C + A\,\cosh^{-2}(x/\lambda)$ (A, C, and λ are all fitting variables) to the same x cut in order to get the halfwidth λ of the electron current sheet. This quantity is shown in Fig. 8 by a blue continuous line. Note that due to the averaging along the z direction, the actual halfwidth of the current sheet at given z slices can be smaller or larger than that value.

This way, Fig. 8 shows that the current sheet halfwidth quickly readjusts due to the initial perturbation and the lack of exact kinetic equilibrium of this force-free current sheet. Also, the initial current sheet is slightly Buneman unstable (cf. Fig. 7). Later, when reconnection is laminar ($t\Omega_{ci} \lesssim 13.5$), the current sheet halfwidth does not change much away from $0.2d_i$. But during the nonlinear evolution ($t\Omega_{ci} \gtrsim 13.5$), when filaments appear, the reconnection rate is greatly enhanced and the spectral indices of the magnetic fluctuations grow beyond -3.0. Then, the halfwidth of the current sheet quickly decreases until it reaches values as low as $0.08d_i$. Meanwhile, the maximum $J_{e,z}$ grows steadily from the beginning, stays more or less constant during the period of laminar reconnection, to quickly grow, finally, during the nonlinear stage of reconnection.

Those instabilities and their turbulence also contribute to the generation of significant deviations in the electron velocity distribution function (EVDF) from the initial drifting Maxwellian. Beams are developed, temperature anisotropies, and even a nongyrotropy of the electron pressure tensor. This is illustrated in Fig. 7(b), showing a cut through the EVDF in the plane v_y-v_z obtained near the X line of reconnection. A double peak is clearly visible in the EVDF, separated by about $4v_{{\rm th},e}$. It is due to the interaction of two counterstreaming beams, providing free energy for a two-streaming instability as well. The origin of those beams can be understood as follows. Originally, the electron distribution function is quite close to a shifted Maxwellian with a drift speed (along z) close to the electron drift speed, which is part of the initial conditions sustaining the current sheet. The reconnection dynamics pulls magnetic flux and thermal electrons (zero drift speed along z) from the upstream region into the X line, bringing together those two populations with a relative drift speed between them. But reconnection also generates a reconnection electric field which accelerates electrons, forming a beamlike population with a very high drift speed and a nonthermal population as well. This also produces an elongated plateau in the $-v_z$ direction, which is a consequence of the nonlinear evolution of the Buneman instability, leading also to beam-driven lower-hybrid instabilities [97,98], contributing to the turbulence near $\Omega_{\rm LH}$.

Thus, while the beam-driven lower-hybrid instability is responsible mainly for the turbulence near the lower-hybrid frequency, Buneman and two-streaming instabilities are behind the high-frequency kinetic turbulence. Since those instabilities should act simultaneously, it is not straightforward to disentangle their individual effects, considering also they should be mainly observed in their saturated state because of their large growth rate and their source of free energy continuously being supplied by magnetic reconnection. This high-frequency turbulence might also quickly change the shape of the EVDFs, but a detailed discussion about those effects is outside of the scope of this paper.

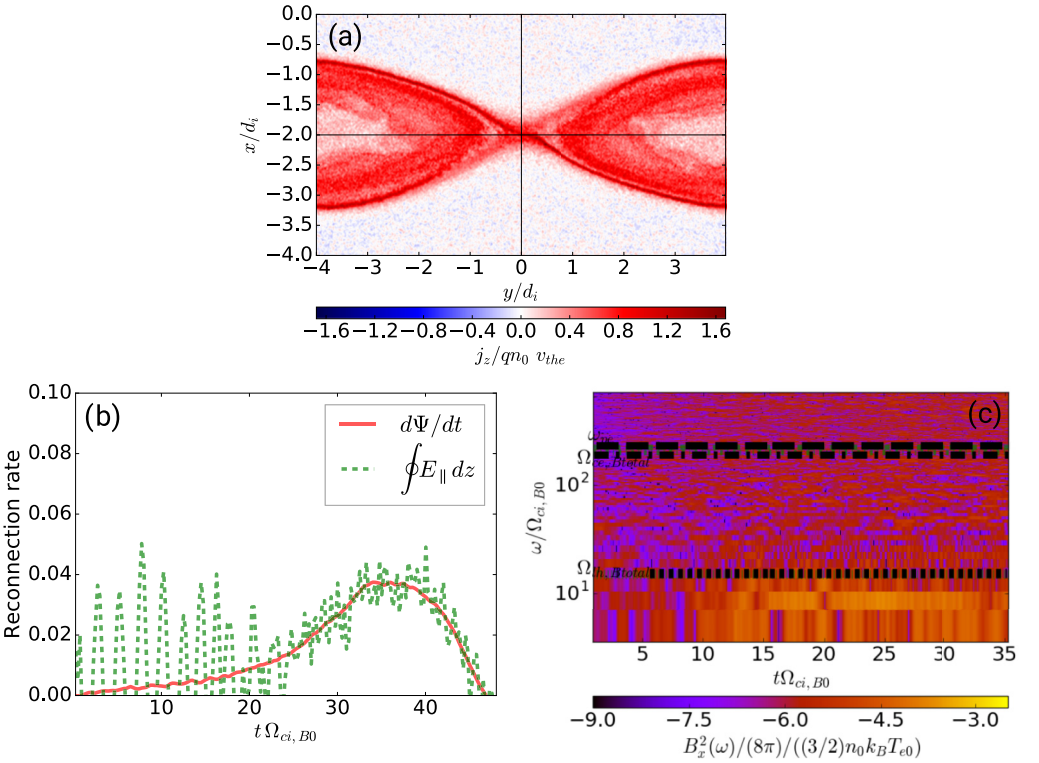

FIG. 9. Results for a simulation run with a current sheet twice as thick and twice as large across the current sheet compared to the original run. (a) Current density J_z at $t\Omega_{ci} = 40$. (b) Normalized reconnection rates. (c) Spectrogram of magnetic fluctuations.

VII. KINETIC TURBULENCE AND RECONNECTION RATES

In our simulations, the presence of high-frequency kinetic turbulence is correlated with enhanced reconnection rates reaching $0.2V_AB_{\infty y}$ and up to $0.5V_AB_{\infty y}$. Although we did not prove a causal relationship, there is some evidence supporting that this association is not only a coincidence. First of all, as has been established for a long time, normalized reconnection rates close to 0.1 are typical for fast reconnection in Harris or force-free current sheets and within a wide range of parameters and physical models, more or less independent on the dissipation mechanism (see, e.g., Refs. [99–101], and references therein). We found here, though, that the reconnection rate can be significantly enhanced by Buneman turbulence, similar to the findings of [81]. This can be interpreted as Buneman turbulence caused anomalous resistivity balancing the reconnection electric field in the framework of a generalized Ohm's law. This requires relatively thin current sheets and fully 3D considerations. That is why such an enhanced reconnection rate was not commonly found in previous simulation studies, but it is within the parameter regime of our study. Therefore, the fact that Buneman instability is present in our simulations and reconnection rates are well above 0.1 hint toward the relation between reconnection rates and this kind of Buneman turbulence.

To support the relation between self-generated (mainly Buneman) turbulence and reconnection rate, we also simulated thicker current sheets (e.g., exactly the double: $L = 0.5d_i$) for otherwise identical parameters. In order to keep the separation constant between the current sheets, we also increased the simulation box length across x to twice its original value. We should mention that by changing the current sheet thickness we are also modifying the stability properties of this system, and so both simulation runs are not completely equivalent. It was found previously that the linear growth rates of the collisionless tearing mode are strongly reduced for thicker current sheets [102,103]. In a just two times thicker current sheet the reduced magnetic field shear implies a relative electron-ion streaming speed below the threshold of the Buneman instability ($v_{\mathrm{th},e}$). As a consequence, no Buneman instability is triggered and the X line does not become turbulent. This can be seen in Fig. 9(a) displaying the out-of-plane current density j_z at fully developed reconnection. Note that the onset of reconnection is delayed because of the thicker current sheet and the larger simulation box size. Figure 9(b) shows that reconnection rates are strongly reduced, with their peak value close to $0.05B_{\infty y}V_A$. This reduction of the reconnection rate is associated with weaker magnetic fluctuations, as can be seen in Fig. 9(c) showing the spectrogram of the perpendicular magnetic field. Different from the original run (see Fig. 3), it is clear that there is no development of a turbulent cascade and the spectral power is not enhanced at all near the lower-hybrid frequency Ω_{LH}. This supports the conjecture that Buneman turbulence enhances reconnection.

VIII. CONCLUSIONS

We have analyzed the properties of self-generated kinetic turbulence by 3D guide-field reconnection in both frequency and wave-number domains. In the course of reconnection, the

self-generated turbulence starts to grow near the lower-hybrid frequency. Later, a broadband spectrum near the lower-hybrid frequency and up to electron frequencies forms, exhibiting a power law with a spectral index of $\alpha \sim -2.8$. Different from previous investigations, we obtained this power-law spectrum of perpendicular magnetic fluctuations directly in the frequency domain for a stationary probe at the X point of reconnection. For comparison purposes, we also analyzed the wave-number spectra in the direction perpendicular to the magnetic field. This also reveals a power-law spectra with a very similar spectral index of $\alpha \sim -2.8$ for $k > \rho_i^{-1}$, but only at times when the normalized reconnection rates are close to 0.1. This wave-number spectral slope further steepens correlated with enhanced reconnection rates above that value. It is also associated with a spectral break close to $k > \rho_i^{-1}$. The similar slope of the ω and k spectra does not necessarily indicate the presence of nondispersive waves with a linear dependence between ω and k_y: we verified that the ω spectrum is different in the outflow regions of reconnection. Those results cannot be directly compared with space observations, but some of the characteristics of this kinetic turbulence have some points in common, as well as with laboratory experiments.

The turbulence above the lower-hybrid frequency is due to kinetic instabilities driven by the streaming of the current carriers, the electrons, their beams, and shear flows. First the Buneman streaming instability starts and later a kinetic electron shear flow instability takes over. These two unstable modes might become coupled [104]. The period of maximum activity of those unstable waves correlates with a fast thinning of the current sheet. The sources of free energy (electron currents and shear flows) are typical for guide-field reconnection. This is in contrast to the limiting case of antiparallel reconnection, where anisotropy-driven and pressure-gradient-driven instabilities prevail. Our results indicate that simulations of magnetic reconnection need to be three-dimensional to accurately describe the intrinsic 3D self-generated turbulence in a real physical current sheet: 2D setups cannot reproduce all the fluctuations and unstable waves seen in realistic environments.

We also provided some evidence that the high-frequency kinetic turbulence generated by streaming and shear flow instabilities is correlated with enhanced reconnection rates. Usually, $0.1 V_A B_{\infty y}$ is considered to be the rate of fast reconnection. However, we showed here that the rate of reconnection through collisionless thin current sheets can be enhanced up to $(0.2\text{–}0.5) V_A B_{\infty y}$ in the presence of Buneman instability. This was also found in a different study [81].

By means of an additional simulation with a thicker current sheet, where Buneman instability is not excited, we showed that the consequent lack of high-frequency turbulence is correlated with weaker reconnection rates on the order of $0.05 V_A B_{\infty y}$. A more concrete and causal proof of this statement would exceed the scope of this paper.

For larger ion to electron mass ratios and initially thicker current sheets, the properties of the dominant instabilities might change. It is very likely that a broadband kinetic turbulence will nevertheless be excited and affect the reconnection process, as laboratory experiments and *in situ* observations have shown. Starting with the current space mission MMS [105] as well as by upcoming new laboratory experiments like FLARE at Princeton, also higher- (electron) frequency turbulence will become observable which might compare better with our simulation results.

ACKNOWLEDGMENTS

We acknowledge the Verein zur Förderung kinetischer Plasmasimulationen e.V. for developing the ACRONYM code and especially Patrick Kilian for his helpful discussions and valuable comments. We further acknowledge the Max-Planck-Princeton Center for Plasma Physics and the DFG Priority Program "Planetary Magnetism" SPP 1488 for support. Computational resources were kindly provided by the PRACE project prj.1602-008 in the Beskow cluster at the PDC/KTH, Sweden. We also used the Hydra cluster of the Max Planck Computing and Data Facility (MPCDF, formerly known as RZG) at Garching, Germany. We also thank the referees for their valuable suggestions that contributed to correct and significantly improve this paper.

APPENDIX: EFFECTS OF NUMERICAL PARAMETERS ON THE FREQUENCY SPECTRA

The numerical noise in PIC simulations might have a strong influence on the turbulence properties of plasmas. This numerical noise depends on parameters like the shape function (interpolation scheme to assign the particles' current to the grid), current smoothing, and especially on the number of particles per cell. We used a second-order triangular-shaped cloud function and a binomial current smoothing to reduce the numerical noise. We also tested that even for four times less particles per cell than the number used here, the frequency spectral index in Fig. 4 is not modified significantly. Indeed, Fig. 10 shows a comparison of the frequency spectra for runs different in only the number of particles per cell. A higher particle count number leads to an even clearer spectral slope with only a slightly different value of the spectral index (-2.8 vs -2.7 in the case with less particles) by increasing the turbulent range before it hits the numerical noise floor at high (electron) frequencies. This numerical noise floor is of course lower when using a higher number of particles.

We also checked that the choice of the time series interval used for the calculation of the frequency spectra has only a slight effect on the spectral index of magnetic fluctuations. Indeed, the spectral index calculated for other intervals like $t\Omega_{ci} = 9\text{–}14$ (instead of $t\Omega_{ci} = 11 - 15$ used here) is -2.7. Therefore, as long as the interval includes the times close to $t\Omega_{ci} = 13.5$, the spectral index is not very sensitive to the choice of time interval for the frequency spectra. We finally chose $t\Omega_{ci} = 11\text{–}15$ in order to include times close to the maximum value of the reconnection rate.

There is another numerical parameter that can affect the value of the spectral index of magnetic fluctuations in the frequency domain: the range used for the linear fit. The lower limit depends on the time series interval: a larger time interval implies the possibility of choosing an even lower frequency limit, but this is constrained by the transient nature of magnetic reconnection in our system, since it would not be meaningful to choose an extended time interval where

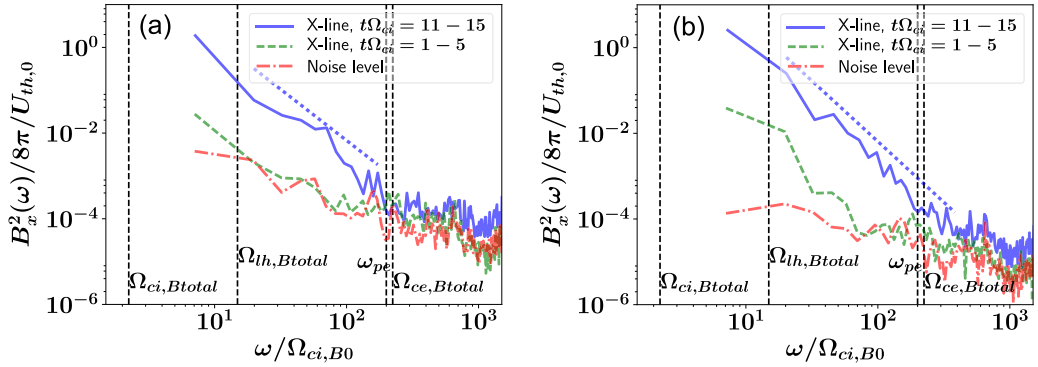

FIG. 10. Spectrum of perpendicular magnetic field fluctuations B_x^2 at the reconnection X point, for two time intervals. (a) Run with 25 particles per cell. (b) Run with 100 particles per cell (results used in this paper; cf. Fig. 4).

reconnection is absent (like at the beginning of our simulation). The lower limit for the fitting also depends on the amount of binning used to smooth the data. Binning and averaging over more data points lead to a smoother spectra but also the lower part of the frequency spectra becomes modified. The values finally chosen in this paper represent a good compromise between those opposite effects. Meanwhile, the upper limit for the range of the linear fit depends on the level of numerical noise. A higher level of numerical noise, like in the case of using less numerical particles, implies that the noise level is higher and therefore the range where a straight line can be fitted in the frequency spectra is shorter. The same effect happens with reduced or no binning used for smoothing the input data. For example, we used here as upper limit $\Omega_{ci,B0}=400$, while without binning (raw data) it is more appropriate to use $\Omega_{ci,B0}=250$.

[1] M. Yamada, R. M. Kulsrud, and H. Ji, Rev. Mod. Phys. **82**, 603 (2010).
[2] R. A. Treumann and W. Baumjohann, Front. Phys. **1**, 1 (2013).
[3] W. H. Matthaeus and S. L. Lamkin, Phys. Fluids **28**, 303 (1985).
[4] A. Lazarian and E. T. Vishniac, Astrophys. J. **517**, 700 (1999).
[5] A. Retinò, D. Sundkvist, A. Vaivads, F. Mozer, M. André, and C. J. Owen, Nat. Phys. **3**, 235 (2007).
[6] D. Sundkvist, A. Retinò, A. Vaivads, and S. D. Bale, Phys. Rev. Lett. **99**, 025004 (2007).
[7] J. T. Gosling, Space Sci. Rev. **172**, 187 (2012).
[8] S. Perri, M. L. Goldstein, J. C. Dorelli, and F. Sahraoui, Phys. Rev. Lett. **109**, 191101 (2012).
[9] K. T. Osman, W. H. Matthaeus, J. T. Gosling, A. Greco, S. Servidio, B. Hnat, S. C. Chapman, and T. D. Phan, Phys. Rev. Lett. **112**, 215002 (2014).
[10] Y. Wang, F. S. Wei, X. S. Feng, X. J. Xu, J. Zhang, T. R. Sun, and P. B. Zuo, Astrophys. J., Suppl. Ser. **221**, 34 (2015).
[11] K. T. Osman, K. H. Kiyani, W. H. Matthaeus, B. Hnat, S. C. Chapman, and Y. V. Khotyaintsev, Astrophys. J. **815**, L24 (2015).
[12] A. Chasapis, A. Retinò, F. Sahraoui, A. Vaivads, Y. V. Khotyaintsev, D. Sundkvist, A. Greco, L. Sorriso-Valvo, and P. Canu, Astrophys. J. **804**, L1 (2015).
[13] Z. Vörös, E. Yordanova, M. M. Echim, G. Consolini, and Y. Narita, Astrophys. J. Lett. **819**, L15 (2016).
[14] E. Yordanova, Z. Vörös, A. Varsani, D. B. Graham, C. Norgren, Y. V. Khotyaintsev, A. Vaivads, E. Eriksson, R. Nakamura, P.-A. Lindqvist, G. Marklund, R. E. Ergun, W. Magnes, W. Baumjohann, D. Fischer, F. Plaschke, Y. Narita, C. T. Russell, R. J. Strangeway, O. Le Contel, C. Pollock, R. B. Torbert, B. J. Giles, J. L. Burch, L. A. Avanov, J. C. Dorelli, D. J. Gershman, W. R. Paterson, B. Lavraud, and Y. Saito, Geophys. Res. Lett. **43**, 5969 (2016).
[15] J. P. Eastwood, T. D. Phan, S. D. Bale, and A. Tjulin, Phys. Rev. Lett. **102**, 035001 (2009).
[16] S. Y. Huang, M. Zhou, F. Sahraoui, A. Vaivads, X. H. Deng, M. André, J. S. He, H. S. Fu, H. M. Li, Z. G. Yuan, and D. D. Wang, Geophys. Res. Lett. **39**, L11104 (2012).
[17] O. Alexandrova, J. Saur, C. Lacombe, A. Mangeney, J. Mitchell, S. J. Schwartz, and P. Robert, Phys. Rev. Lett. **103**, 165003 (2009).
[18] C. H. K. Chen, S. Boldyrev, Q. Xia, and J. C. Perez, Phys. Rev. Lett. **110**, 225002 (2013).
[19] C. H. K. Chen, L. Leung, S. Boldyrev, B. A. Maruca, and S. D. Bale, Geophys. Res. Lett. **41**, 8081 (2014).
[20] S. Bourouaine, O. Alexandrova, E. Marsch, and M. Maksimovic, Astrophys. J. **749**, 102 (2012).
[21] R. Bruno and L. Trenchi, Astrophys. J. **787**, L24 (2014).
[22] S. Boldyrev, C. H. K. Chen, Q. Xia, and V. Zhdankin, Astrophys. J. **806**, 238 (2015).
[23] H. Breuillard, E. Yordanova, A. Vaivads, and O. Alexandrova, Astrophys. J. **829**, 54 (2016).
[24] S. D. Bale, P. J. Kellogg, F. S. Mozer, T. S. Horbury, and H. Reme, Phys. Rev. Lett. **94**, 215002 (2005).
[25] C. H. K. Chen, S. D. Bale, C. Salem, and F. S. Mozer, Astrophys. J. **737**, L41 (2011).
[26] F. S. Mozer and C. H. K. Chen, Astrophys. J. **768**, L10 (2013).
[27] L. Matteini, O. Alexandrova, C. H. K. Chen, and C. Lacombe, Mon. Not. R. Astron. Soc. **466**, 945 (2017).
[28] C. H. K. Chen, C. S. Salem, J. W. Bonnell, F. S. Mozer, and S. D. Bale, Phys. Rev. Lett. **109**, 035001 (2012).
[29] C. H. K. Chen, L. Sorriso-Valvo, J. Šafránková, and Z. Němeček, Astrophys. J. **789**, L8 (2014).

[30] J. Šafránková, Z. Nemecek, F. Nemec, L. Prech, A. Pitna, C. H. K. Chen, and G. N. Zastenker, Astrophys. J. **803**, 107 (2015).

[31] J. J. Podesta, D. A. Roberts, and M. L. Goldstein, J. Geophys. Res. **111**, A10109 (2006).

[32] J. Šafránková, Z. Němeček, L. Prech, and G. N. Zastenker, Phys. Rev. Lett. **110**, 025004 (2013).

[33] J. Šafránková, Z. Nemecek, F. Nemec, L. Prech, C. H. K. Chen, and G. N. Zastenker, Astrophys. J. **825**, 121 (2016).

[34] T. A. Carter, M. Yamada, H. Ji, R. M. Kulsrud, and F. Trintchouk, Phys. Plasmas **9**, 3272 (2002).

[35] W. Fox, M. Porkolab, J. Egedal, N. Katz, and A. Le, Phys. Plasmas **17**, 072303 (2010).

[36] A. von Stechow, O. Grulke, and T. Klinger, Plasma Phys. Controlled Fusion **58**, 014016 (2015).

[37] R. J. Leamon, C. W. Smith, N. F. Ness, and H. K. Wong, J. Geophys. Res.: Space Phys. **104**, 22331 (1999).

[38] T. Passot and P. L. Sulem, Astrophys. J. Lett. **812**, L37 (2015).

[39] O. Stawicki, S. P. Gary, and H. Li, J. Geophys. Res. **106**, 8273 (2001).

[40] G. G. Howes, S. C. Cowley, W. Dorland, G. W. Hammett, E. Quataert, and A. A. Schekochihin, J. Geophys. Res. **113**, A05103 (2008).

[41] S. Boldyrev, K. Horaites, Q. Xia, and J. C. Perez, Astrophys. J. **777**, 41 (2013).

[42] S. P. Gary, J. Geophys. Res.: Space Phys. **104**, 6759 (1999).

[43] F. Sahraoui, M. L. Goldstein, P. Robert, and Y. V. Khotyaintsev, Phys. Rev. Lett. **102**, 231102 (2009).

[44] F. Sahraoui, S. Y. Huang, G. Belmont, M. L. Goldstein, A. Rétino, P. Robert, and J. De Patoul, Astrophys. J. **777**, 15 (2013).

[45] S. Y. Huang, F. Sahraoui, X. H. Deng, J. S. He, Z. G. Yuan, M. Zhou, Y. Pang, and H. S. Fu, Astrophys. J. **789**, L28 (2014).

[46] G. I. Taylor, Proc. R. Soc. A **164**, 476 (1938).

[47] K. G. Klein, G. G. Howes, and J. M. TenBarge, Astrophys. J. Lett. **790**, L20 (2014).

[48] K. G. Klein, J. C. Perez, D. Verscharen, A. Mallet, and B. D. G. Chandran, Astrophys. J. **801**, L18 (2015).

[49] G. G. Howes, W. Dorland, S. C. Cowley, G. W. Hammett, E. Quataert, A. A. Schekochihin, and T. Tatsuno, Phys. Rev. Lett. **100**, 065004 (2008).

[50] T. N. Parashar, M. A. Shay, P. A. Cassak, and W. H. Matthaeus, Phys. Plasmas **16**, 032310 (2009).

[51] A. Greco, F. Valentini, S. Servidio, and W. H. Matthaeus, Phys. Rev. E **86**, 066405 (2012).

[52] F. Valentini, S. Servidio, D. Perrone, F. Califano, W. H. Matthaeus, and P. Veltri, Phys. Plasmas **21**, 082307 (2014).

[53] L. Franci, S. Landi, L. Matteini, A. Verdini, and P. Hellinger, Astrophys. J. **812**, 21 (2015).

[54] S. Servidio, F. Valentini, D. Perrone, A. Greco, F. Califano, W. H. Matthaeus, and P. Veltri, J. Plasma Phys. **81**, 325810107 (2015).

[55] A. B. Navarro, B. Teaca, D. Told, D. Groselj, P. Crandall, and F. Jenko, Phys. Rev. Lett. **117**, 245101 (2016).

[56] T. N. Parashar and W. H. Matthaeus, Astrophys. J. **832**, 57 (2016).

[57] S. S. Cerri and F. Califano, New J. Phys. **19**, 025007 (2017).

[58] L. Franci, S. S. Cerri, F. Califano, S. Landi, E. Papini, A. Verdini, L. Matteini, F. Jenko, and P. Hellinger, Astrophys. J. **850**, L16 (2017).

[59] M. Wan, W. H. Matthaeus, H. Karimabadi, V. Roytershteyn, M. A. Shay, P. Wu, W. Daughton, B. Loring, and S. C. Chapman, Phys. Rev. Lett. **109**, 195001 (2012).

[60] P. Wu, S. Perri, K. Osman, M. Wan, W. H. Matthaeus, M. A. Shay, M. L. Goldstein, H. Karimabadi, and S. Chapman, Astrophys. J. **763**, L30 (2013).

[61] H. Karimabadi, V. Roytershteyn, M. Wan, W. H. Matthaeus, W. Daughton, P. Wu, M. A. Shay, B. Loring, J. Borovsky, E. Leonardis, S. C. Chapman, and T. K. M. Nakamura, Phys. Plasmas **20**, 012303 (2013).

[62] C. T. Haynes, D. Burgess, and E. Camporeale, Astrophys. J. **783**, 38 (2014).

[63] M. Wan, W. H. Matthaeus, V. Roytershteyn, H. Karimabadi, T. Parashar, P. Wu, and M. A. Shay, Phys. Rev. Lett. **114**, 175002 (2015).

[64] D. Grošelj, A. Mallet, N. F. Loureiro, and F. Jenko, Phys. Rev. Lett. **120**, 105101 (2018).

[65] D. Grošelj, S. S. Cerri, A. B. Navarro, C. Willmott, D. Told, N. F. Loureiro, F. Califano, and F. Jenko, Astrophys. J. **847**, 28 (2017).

[66] G. G. Howes, Philos. Trans. R. Soc., A **373**, 20140145 (2015).

[67] A. Mallet, A. A. Schekochihin, and B. D. G. Chandran, J. Plasma Phys. **83**, 905830609 (2017).

[68] A. Mallet, A. A. Schekochihin, and B. D. G. Chandran, Mon. Not. R. Astron. Soc. **468**, 4862 (2017).

[69] N. F. Loureiro and S. Boldyrev, Phys. Rev. Lett. **118**, 245101 (2017).

[70] N. F. Loureiro and S. Boldyrev, Astrophys. J. **850**, 182 (2017).

[71] S. Boldyrev and N. F. Loureiro, Astrophys. J. **844**, 125 (2017).

[72] W. H. Matthaeus, M. Wan, S. Servidio, A. Greco, K. T. Osman, S. Oughton, and P. Dmitruk, Philos. Trans. R. Soc., A **373**, 20140154 (2015).

[73] Y.-M. Huang and A. Bhattacharjee, Astrophys. J. **818**, 20 (2016).

[74] E. Leonardis, S. C. Chapman, W. Daughton, V. Roytershteyn, and H. Karimabadi, Phys. Rev. Lett. **110**, 205002 (2013).

[75] J. Büchner and J. Kuska, Ann. Geophys. **17**, 604 (1999).

[76] I. Silin and J. Büchner, Phys. Plasmas **10**, 3561 (2003).

[77] I. Silin and J. Büchner, Phys. Plasmas **10**, 1299 (2003).

[78] J. Büchner and N. Elkina, Space Sci. Rev. **121**, 237 (2005).

[79] J. Büchner and N. Elkina, Phys. Plasmas **13**, 082304 (2006).

[80] H. Che, J. F. Drake, and M. Swisdak, Nature (London) **474**, 184 (2011).

[81] H. Che, Phys. Plasmas **24**, 082115 (2017).

[82] P. A. Muñoz, J. Büchner, and P. Kilian, Phys. Plasmas **24**, 022104 (2017).

[83] J. F. Drake, M. Swisdak, C. Cattell, M. A. Shay, B. N. Rogers, and A. Zeiler, Science **299**, 873 (2003).

[84] Y.-H. Liu, W. Daughton, H. Karimabadi, H. Li, and V. Roytershteyn, Phys. Rev. Lett. **110**, 265004 (2013).

[85] L. Price, M. Swisdak, J. F. Drake, P. A. Cassak, J. T. Dahlin, and R. E. Ergun, Geophys. Res. Lett. **43**, 6020 (2016).

[86] L. Price, M. Swisdak, J. F. Drake, J. L. Burch, P. A. Cassak, and R. E. Ergun, J. Geophys. Res.: Space Phys. **122**, 11,086 (2017).

[87] J. Büchner, Plasma Phys. Controlled Fusion **49**, B325 (2007).

[88] P. A. Muñoz, D. Told, P. Kilian, J. Büchner, and F. Jenko, Phys. Plasmas **22**, 082110 (2015).

[89] P. Kilian, T. Burkart, and F. Spanier, in *High Performance Computing in Science and Engineering '11*, edited by W. E. Nagel, D. B. Kröner, and M. M. Resch (Springer, Berlin/Heidelberg, 2012), pp. 5–13.
[90] P. Dmitruk and W. H. Matthaeus, Phys. Plasmas **16**, 062304 (2009).
[91] J. M. TenBarge and G. G. Howes, Phys. Plasmas **19**, 055901 (2012).
[92] S. S. Cerri, F. Califano, F. Jenko, D. Told, and F. Rincon, Astrophys. J. **822**, L12 (2016).
[93] O. Buneman, Phys. Rev. Lett. **1**, 8 (1958).
[94] P. A. Muñoz and J. Büchner, Phys. Plasmas **23**, 102103 (2016).
[95] G. Ganguli, Y. C. Lee, and P. J. Palmadesso, Phys. Fluids **31**, 823 (1988).
[96] H. Romero, G. Ganguli, Y. C. Lee, and P. J. Palmadesso, Phys. Fluids B **4**, 1708 (1992).
[97] B. F. McMillan and I. H. Cairns, Phys. Plasmas **13**, 052104 (2006).
[98] B. F. McMillan and I. H. Cairns, Phys. Plasmas **14**, 012103 (2007).
[99] L. Comisso and A. Bhattacharjee, J. Plasma Phys. **82**, 595820601 (2016).
[100] Y.-H. Liu, M. Hesse, F. Guo, W. Daughton, H. Li, P. A. Cassak, and M. A. Shay, Phys. Rev. Lett. **118**, 085101 (2017).
[101] P. A. Cassak, Y.-H. Liu, and M. A. Shay, J. Plasma Phys. **83**, 715830501 (2017).
[102] P. L. Pritchett, F. V. Coroniti, R. Pellat, and H. Karimabadi, J. Geophys. Res. **96**, 11523 (1991).
[103] M. Brittnacher, K. B. Quest, and H. Karimabadi, J. Geophys. Res. **100**, 3551 (1995).
[104] H. Che, M. V. Goldman, and D. L. Newman, Phys. Plasmas **18**, 052109 (2011).
[105] J. L. Burch *et al.*, Science **352**, aaf2939 (2016).